Testing an in-line digital holography 'inverse method' for the Lagrangian tracking of evaporating droplets in homogeneous nearly isotropic turbulence

Delphine Chareyron, Jean-Louis Marié, Corinne Fournier, Jérôme Gire,
Nathalie Grosjean, Loïc Denis, Michel Lance, Loïc Méès

HAL is a multi-disciplinary open access archive for the deposit and dissemination of scientific research documents, whether they are published or not. The documents may come from teaching and research institutions in France or abroad, or from public or private research centers.

L'archive ouverte pluridisciplinaire **HAL**, est destinée au dépôt et à la diffusion de documents scientifiques de niveau recherche, publiés ou non, émanant des établissements d'enseignement et de recherche français ou étrangers, des laboratoires publics ou privés.

Testing an in-line digital holography 'inverse method' for the Lagrangian tracking of evaporating droplets in homogeneous nearly isotropic turbulence

D Chareyron[1,4]**, J L Marié**[1,5]**, C Fournier**[2]**, J Gire**[2]**, N Grosjean**[1]**, L Denis**[3] **and L Méès**[1]

[1] Laboratoire de Mécanique des Fluides et d'Acoustique UMR5509, Ecole Centrale de Lyon—CNRS—Université Claude Bernard Lyon 1—INSA Lyon, 36 avenue Guy de Collongue, 69134 Ecully Cedex, France
[2] Laboratoire Hubert Curien UMR5516, CNRS—Université Jean-Monnet, 18 rue Pr Benoit Lauras, F-42000, St Etienne, France
[3] Centre de Recherche Astronomique de Lyon UMR5574, CNRS—ENSL—Université Claude Bernard Lyon 1, France
E-mail: jean-louis.marie@ec-lyon.fr

Abstract. An in-line digital holography technique is tested, the objective being to measure Lagrangian three-dimensional (3D) trajectories and the size evolution of droplets evaporating in high-Re_λ strong turbulence. The experiment is performed in homogeneous, nearly isotropic turbulence ($50 \times 50 \times 50 \, \text{mm}^3$) created by the meeting of six synthetic jets. The holograms of droplets are recorded with a single high-speed camera at frame rates of 1–3 kHz. While hologram time series are generally processed using a classical approach based on the Fresnel transform, we follow an 'inverse problem' approach leading to improved size and 3D position accuracy and both in-field and out-of-field detection. The reconstruction method is validated with 60 μm diameter water droplets released from a piezoelectric injector 'on-demand' and which do not appreciably evaporate in the sample volume. Lagrangian statistics on 1000 reconstructed tracks are presented. Although improved, uncertainty on the depth positions remains higher, as expected in in-line digital holography. An additional filter is used to reduce the effect of this uncertainty when calculating the droplet

[4] Present address: Laboratoire de Physique de l'ENSL, UMR5672 CNRS, 46 Allée d'Italie, 69364 Lyon Cedex 07, France.
[5] Author to whom any correspondence should be addressed.

velocities and accelerations along this direction. The diameters measured along the trajectories remain constant within $\pm 1.6\%$, thus indicating that accuracy on size is high enough for evaporation studies. The method is then tested with R114 freon droplets at an early stage of evaporation. The striking feature is the presence on each hologram of a thermal wake image, aligned with the relative velocity fluctuations 'seen' by the droplets (visualization of the Lagrangian fluid motion about the droplet). Its orientation compares rather well with that calculated by using a dynamical equation for describing the droplet motion. A decrease of size due to evaporation is measured for the droplet that remains longest in the turbulence domain.

Contents

1. Introduction

The evaporation of droplets transported by a turbulent flow is a physical phenomenon encountered in many practical situations. It has been intensively studied in the past in various contexts: spray dryers, fuel injection for combustion chambers, atmospheric dispersion and physics of clouds. The complexity of these flows arises from the coupling that exists between the evaporation process and the turbulent dispersion. As they interact with the turbulence eddies of the carrier phase, droplets disperse with different three-dimensional (3D) trajectories and are subjected to different surrounding relative velocity fluctuations during their motion. These relative fluctuations influence the local convective heat transfer, so that each droplet evaporates more rapidly or slowly depending on the trajectory it follows. Moreover, depending on their characteristic Stokes number, droplets may concentrate in preferential regions and form clusters [1], which also influences the evaporation [2]. Both processes contribute to rendering their initial size distribution more polydispersed. At the same time, the evolution in diameter caused by the evaporation modifies the force acting on the droplets and thus their trajectories in a complex way. The dynamics of droplets, which are non-neutrally buoyant particles, is

affected by inertia and so differs from that of fluid particles. But as the droplets evaporate, they become smaller and smaller compared to the relevant scales of the turbulence and, at the limit, can approach the behaviour of passive tracers. It is difficult to investigate this coupling between evaporation and turbulence in real situations, where it is combined with other effects (coalescence, breakup, wall interactions, etc). Besides, the Eulerian measuring techniques that are used in most studies on dispersion–evaporation are not best suited for providing a complete understanding of physical mechanisms involved [3]. Our objective is to obtain experimental information on this coupling from a Lagrangian point of view in a simpler, fundamental situation, where the important parameters of the problem (the Lagrangian time scale of turbulence, the response and evaporation times of the droplets) can be controlled. Practically, the experiment consists in releasing a dilute train of monodispersed droplets in a homogeneous, nearly isotropic strong turbulence and measuring their size evolution in conjunction with their trajectories and spatial dispersion. This paper focuses on the measuring technique that has been selected for this study.

Most Lagrangian techniques are recent: about 15 years old or less, and have essentially been used to investigate the dispersion of particles in turbulent flows. A detailed survey can be found in the review paper by Toschi and Bodenschatz [4]. They are based on various principles such as 3D particle tracking velocimetry (3D PTV) with four cameras [5, 6], optical imaging with silicon strip detectors [7–10], extended laser Doppler anemometry (extended LDA) [11], ultrasonic Doppler tracking [12] and digital holography [13–15]. Compared to the other techniques mentioned, the main advantage of digital holography is that it provides information on size, which is obviously crucial for evaporation studies and caused us to select it. The method that has been chosen is an in-line digital holography setup. This setup is well suited to Lagrangian measurements in flows with low concentrations of particles [16, 17], which is typically the case here (see section 2.2). Moreover, it is insensitive to vibrations and easy to implement, two important points for our operating conditions. The in-line digital holography method has already been proved to be successful in studying the turbulent dispersion of slightly buoyant droplets in homogeneous, nearly isotropic turbulence with high-speed cameras [13, 18]. However, the rms velocity fluctuations in this case are low, of the order of $10\,\mathrm{cm\,s^{-1}}$, and no phase change takes place. The situation that most resembles ours is that explored by Lu *et al* [14]. These authors tested an in-line single high-speed camera method on droplets dispersing in strong turbulence within a box [19] and compared its accuracy to that of a stereo setup with two high-speed cameras. They showed that the in-line method is capable of measuring particle size and trajectories in this type of flow, and that it has certain advantages compared to the stereo method: simplified setup and calibration, need of less laser power, no particle-matching between cameras and a deeper sample volume (even for small numerical aperture experiments). From their results, obtained with a standard hologram reconstruction method, a number of limitations of in-line digital holography can be listed.

- The spatial resolution along the optical axis is poor (about 100 times lower than in the transverse directions). This yields a poor estimation of particle acceleration along this axis.
- The sample volume is small in the transverse directions: 17.6 mm × 13.2 mm (for a setup without magnification, the lateral field of view is restricted to the width of the sensor).
- The sizing accuracy along the tracks is found to be of the order of ±10% with a simple sizing algorithm (pixel-counting), which is still far from the accuracy of other local techniques such as phase Doppler anemometry (PDA).

As emphasized by many authors, there are several ways to push back these limits. One of them is to use improved algorithms for digital hologram processing. An 'inverse problem' approach dedicated to 3D reconstructions of objects with simple parametric shapes (most notably, droplets modelled by spheres) has recently been proposed [20–22] and tested both on simulated data and on a jet of monodispersed droplets. This approach proves particularly promising to address some of the main issues encountered in in-line holography today. The proposed algorithm improves depth positioning accuracy, provides particle diameters with sub-micrometer accuracy, eliminates bias close to the hologram border and increases the volume of the reconstructed domain [23]. The purpose of this work, therefore, is to apply this approach to our highly turbulent flow and show that it retains its performance in real conditions. The method is tested with water droplets (the case exhibiting no appreciable evaporation) and freon droplets (the case with potential evaporation). The paper is organized as follows. First we describe the experimental setup, including the system generating the turbulence, the droplet injectors, the conditioning freon circuit and the digital in-line holography setup. Then the algorithms used to process the holograms are detailed. Finally, the results obtained in the two cases are presented and interesting aspects of the method for the Lagrangian evaporation study are discussed. The conclusion summarizes the most important points of this work.

2. Experimental setup

2.1. Turbulence facility

The experiment has been performed in homogeneous isotropic turbulence whose detailed characterization can be found in [24]. The facility, inspired by the original idea of Hwang and Eaton [19], consists of an 'open' turbulence chamber displayed in figure 1. Turbulence is produced by the mixing of six large synthetic jets, in an ambient atmosphere. The jets are created by six loudspeakers which are mounted on the lateral sides of a $0.9\,\text{m}^2$ cubic frame, so as to form the vertices of a regular octahedron. Unlike the chamber designed by Hwang and Eaton there are no walls, which has some advantages for the present study, in particular as confinement is almost non-existent, no significant secondary motions take place outside the quasi-isotropic turbulence. As a result, the probability of droplets that leave this domain of interest re-entering the domain is almost nil. This is an essential requirement for experiments where the coupling between the evaporation process and turbulence dispersion is studied. From a practical point of view, the absence of walls is favourable for optical techniques such as digital holography, as an important source of noise, such as fringes created by interference on the glass windows, is avoided. Each loudspeaker is driven with sine waves with the same 42 Hz frequency and phase. The balance between the six loudspeakers is optimized at the beginning of the experiment by adjusting the driving signals, so as to obtain zero average velocities and equal fluctuations in the X and Y directions. This is checked by LDA measurements at the centre of the domain ($X = Y = Z = 0$).

The measurements presented in the next sections have been taken in turbulence with a Reynolds number based on the Taylor scale $Re_\lambda = 293$. The properties of this turbulence were measured by particle image velocimetry (PIV), as described in [24]. The domain where turbulence is homogeneous, nearly isotropic, is a cube whose side L_{TD} is about 50 mm. The mean flow velocity, the rms turbulence fluctuations and the integral length scale are of the order of $0.04\,\text{ms}^{-1}$, $0.9\,\text{ms}^{-1}$ and 45 mm, respectively. The statistical characteristics and scales of
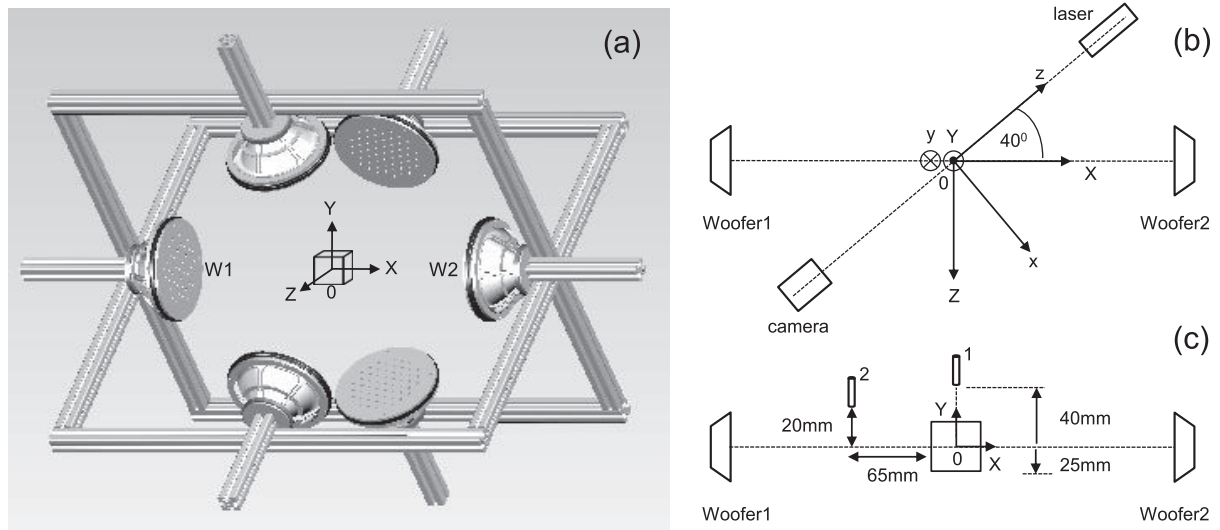
Figure 1. (a) Schematic diagram of the turbulence-generating system. The homogeneous isotropic domain is approximately a cube with $L_{TD} = 50$ mm sides located at the centre; (O, X, Y, Z) denote the axes of reference for the domain; (b) layout of the holographic setup in the plane X–Z; (O, x, y, z) denote the axes of reference attached to the optical setup, with z being the optical axis. (c) Locations of the droplet generator: 1, the case of water; 2, the case of freon.

**Table 1.** Turbulence characteristics.

Twice the kinetic energy q^2 (m² s⁻²)	Dissipation rate ϵ (m² s⁻³)	Taylor microscale λ (mm)	Reynolds number Re_λ	Turnover time T_E (ms)	Integral length scale Λ (mm)	Kolmogorov	
						length scale η_k (mm)	time τ_k (ms)
2.12	5.78	5.2	293	56	47	0.16	1.60
error estimates							
4–5%	20%	11%	13%	20%	15–20%	5%	9%

the turbulence are summarized in table 1. The Lagrangian time scale T_L, characteristic of the exponential decrease of the Lagrangian gas velocity autocorrelation, could not be measured directly. It was estimated both from the eddy-turnover time $T_E \approx 0.5\, q^2/(3\epsilon)$ and from the Kolmogorov time $\tau_k = (\nu/\epsilon)^{0.5}$. Referring to [25–27], $T_L/T_E \approx 0.76$–0.78 and $T_L/\tau_k \approx 20$–24 for the Re_λ investigated here. This yields a value of T_L in the 32–45 ms range.

2.2. Injection system

For the evaporation of droplets to be investigated from a Lagrangian point of view, one must be able to measure their diameter along the 3D trajectories. To show that the in-line holographic method allows this measurement with a good degree of confidence, it was tested with monodispersed droplets, well controlled in size.

The droplets are generated with a piezoelectric MJ-AT-01 jetting device manufactured by MicroFab Technologies (figure 2(a)). This device consists of a glass capillary with a $60\,\mu m$

(a)　　　　　　　　　　　　(b)
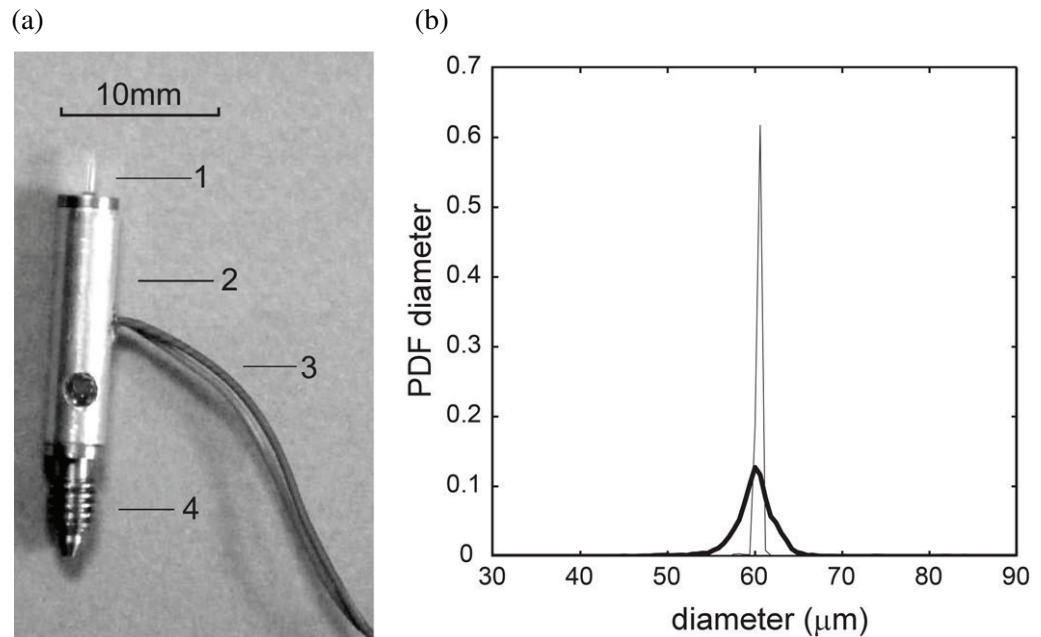
Figure 2. (a) Photograph of the MJ-AT-01 injector MicroFab Technologies. 1: Glass capillary; 2: metallic case; 3: connections for the piezoceramic; 4: threaded end. (b) PDF water droplet's diameter as measured by PDA without turbulence (thin line) and with turbulence (thick line).

orifice diameter (1), embedded in a piezoceramic tube. This kind of injector has the advantage of being miniaturized, but also of enabling two types of functioning. It can work either in a commonly known 'continuous droplet jet-mode' or in a 'droplet-on-demand mode' [28, 29]. The on-demand mode has been adopted here because it provides monodispersed droplets with a stable size over long periods of time (a few hours) and which are pretty well reproduced from one run to the next. The droplets thus generated have approximately the same diameter as that of the glass capillary, i.e. about $60\,\mu$m.

This diameter has been chosen so that the response time τ_d of the droplets is around T_L for the fluids used in the study, which is the condition for significant coupling to take place. The fluids are demineralized water, which does not evaporate appreciably on the residence time scales, and freon R114 whose boiling point is $3.8°$C under atmospheric pressure. The water was used as a test fluid to show that trajectories and diameters could be measured with high accuracy with our digital holography technique. In particular, it was verified that, since there is no appreciable evaporation in this case, the diameters along each track remain constant. The typical response times are of the order of 10–20 ms, which yields a Stokes number $St_k = \tau_d/\tau_k \approx 6.5$–12.5. Droplets are generated at a frequency of $500\,$Hz. The monodispersed character of the droplets has been checked in the case of water by measuring their size at the outlet of the injector with a PDA system. The results reported in figure 2(b) and table 2 confirm that size distribution peaks well around a $62\,\mu$m mean diameter within $\pm0.5\,\mu$m. The velocity of the droplets at the outlet is typically $1.2\,$ms^{-1}. The mean diameter may slightly vary from one run to the next in the range $60 \pm 2\,\mu$m, but the standard deviation of the size distribution remains unchanged. The droplets thus generated are about half of the Kolmogorov scale ($0.4\eta_k$).

Table 2. Droplet characteristics.

Flow	Average diameter d (μm)	rms diameter σ_d (μm)
Without turbulence	61.7	0.5
With turbulence	60.1	2.6

The droplets are injected above the homogeneous isotropic domain into a point on the vertical Y-axis ($X = Z = 0$ mm) located at a distance of 40 mm from the centre of the domain (location 1 in figure 1(c)). This location has been adopted because it respects the symmetry of the loudspeakers and minimizes the flow disturbance. The distance to the centre has been selected by compromise. On the one hand, the velocity of the droplets entering the turbulence domain must not be too high compared with the turbulent velocity fluctuations. On the other hand, their momentum must be sufficient to allow them to penetrate the domain.

$Y = 40$ mm is reasonable to fulfil both conditions. Simple considerations based on the droplet dynamical equation show that a 60 μm water droplet injected there penetrates the domain at $Y = 25$ mm with a velocity of the order of magnitude of the turbulence fluctuations and reaches its settling velocity inside the domain. If the distance is too great most of the droplets are expelled outside the domain and in this case samples are definitely too few to make acceptable statistics during the length of time when loudspeakers are stable, typically 60 min [24]. This kind of difficulty arises from the non-confinement and the fact that the number of droplets delivered by the injector is limited. It is not encountered in closed turbulence chambers [14, 30], where particles or drops are introduced with their settling velocity in much higher concentrations and remain captured inside the box. With the compromise adopted here, 4% of the droplets released penetrate the turbulence domain.

The penetration rate has been measured by using the interferometric laser imaging for droplet sizing (ILIDS) technique. It has been shown that it was possible to increase the penetration rate up to 13% by injecting from the lateral side ($X = -90$ mm, $Y = 20$ mm, $Z = 0$ mm) facing one of the loudspeakers, so that the turbulent jet arriving there drives them more easily into the turbulence domain (location 2 in figure 1(c)). However, this location being comparatively more intrusive, it was not used for the holographic tests with water droplets. PDA measurements of the droplet size have been made at the centre of the domain with the injector at location 1. We see in figure 2(b) that the size distribution is slightly broader than when measured immediately at the outlet of the injector without turbulence (table 2). As was checked by ILIDS, this broadening is not a measuring bias associated with the location of the PDA volume relative to the injector: at the outlet or far from it. It is more likely caused by the fact that turbulence strongly destabilizes the jet of droplets close to the tip of the capillary and, by doing so, influences the droplet formation.

As the droplets are injected at a frequency of 500 Hz, their average number N_d in the turbulence domain is estimated to be $500\tau_r$, where τ_r is their mean residence time inside this domain. τ_r is about 13.3 ms (see section 4.1), which yields $N_d \approx 7$. This number is consistent with the number of droplets recorded on average per hologram (figure 7(a)). The droplet number density $n_d = N_d/L_{TD}^3$ is thus very low, of the order of 0.06 cm^{-3}, and far below the limit at which speckle-noise on the holograms becomes excessive for in-line holography [31]. According to the
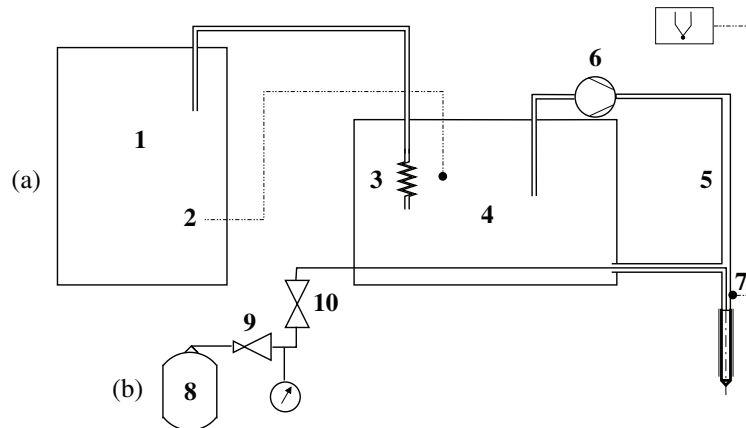
Figure 3. Temperature conditioning for the injection of freon R114. (a) Cooling circuit; 1: TC50E Huber immersion cooler; 2: adjustment of the cooling set-point temperature; 3: serpentine exchanger; 4: refrigerant bath; 5: recirculating cooling tube, 6: peristaltic pump; 7: thermocouple for measuring the temperature at injection. (b) Injection circuit; 8: R114 pressurized tank; 9: DL-BP1 high-precision pressure-reducing valve for cryogenic fluids; 10: Mastercool pressure reducing valve.

shadow density criterion of Royer [32], the limit for obtaining high-quality holograms with our parameters (the diameter of the droplets and size of the sample volume) is $n_\mathrm{d} = 50\,\mathrm{cm}^{-3}$.

2.3. Freon conditioning circuit

Freon R114 is stored in a high-pressure tank and first had to be liquefied before being injected at atmospheric pressure. This requires decreasing the temperature below $0\,^\circ$C, and for that reason, a special supply device was designed to achieve the phase change and transport the R114 in its liquid form up to the nozzle. Basically, the device consists of two separate circuits (figure 3). The cooling circuit (a) necessary for the phase change and for keeping the R114 liquid includes an immersion cooler (1), a serpentine exchanger (3) and a refrigerant bath (4), whose cooling set point is adjusted by a controller (2). The refrigerant of the bath (R290) is recirculated by a peristaltic pump (6) in a 8 mm diameter silicon tube (5) up to the glass capillary, from where it then returns to the bath. The temperature of the R114 is measured at the entrance of the capillary by a thermocouple (7). The injection circuit (b) includes the R114 pressurized tank (8), a high-precision pressure-reducing valve for cryogenic fluids (9) and a mastercool pressure-reducing valve (10). The R114 is depressurized down to atmospheric pressure, enters the cooling bath where it is liquefied and is driven up to the nozzle. The injection pressure is adjusted by (9) with an accuracy of 5 mbar. The set-point temperature of the cooling bath is typically $-10\,^\circ$C, while the temperature of the R114 just before injection is $-5\,^\circ$C. The size of the R114 droplets could not be so well controlled as that of water droplets, due to some instabilities in the injection circuit and the appearance of hoarfrost on the capillary tip. In this case, the droplets are no longer monodispersed and are on average somewhat larger, of the order of 240 μm (see figure 4). In order to facilitate their penetration into the domain, they were injected from location 2 (figure 1(c)).
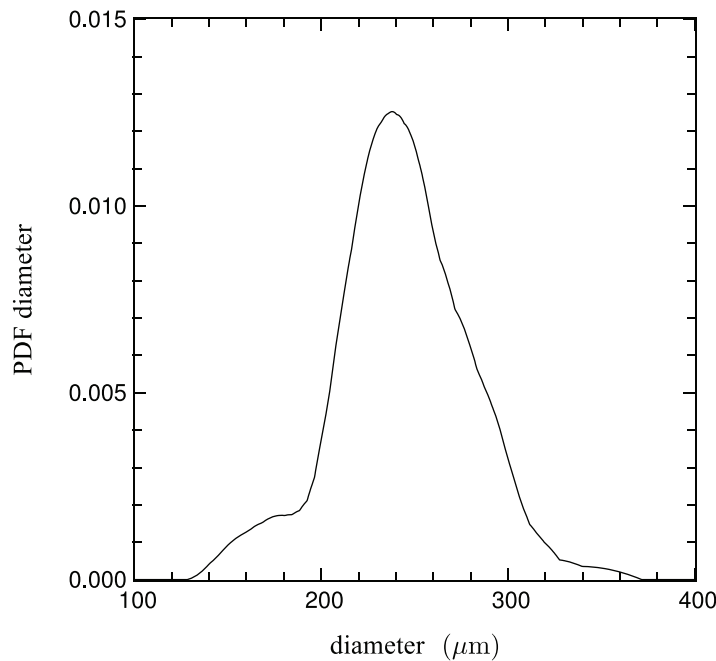
Figure 4. PDF of the freon droplets' initial diameters. Statistics on 63 droplets. Mean diameter: 243 μm; standard deviation: 33 μm.
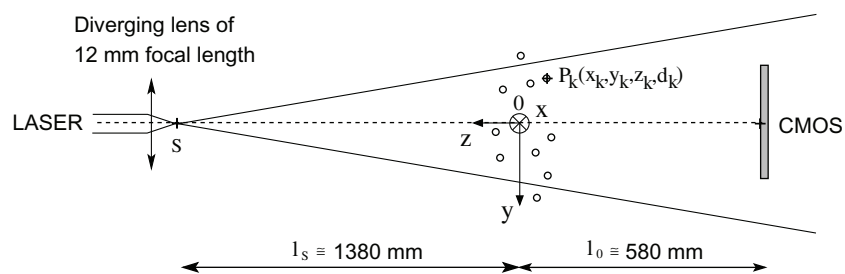
Figure 5. Schematic diagram of the in-line holography setup.

2.4. Digital in-line holography setup—tracking method

The turbulence domain is illuminated by a Millenia IIs Spectra Physics solid laser (see figure 5), emitting coherent light at $\lambda_{\text{laser}} = 532$ nm. The optical axis z of the source is positioned in the plane X–Z of the domain, at an angle of $40°$ to the X-axis (see figure 1(b)). This angle proves to be necessary for good optical access to the domain of interest. The beam at the laser outlet is expanded by a 12 mm diverging lens located 1380 mm from the plane where water droplets are injected (($x, y, z = 0$) in figure 1(b)). The uniformity of the obtained wave front was found satisfactory and thus no spatial filter was added. The sensor of the camera is placed in front of the source, 580 mm from the injection plane.

The slight beam divergence (about $4°$) that results causes a magnification, improving the signal-to-noise ratio of the holograms (the magnitude of a diffraction pattern without magnification is proportional to d^2/z, and to $G^2 d^2/Gz = G d^2/z$ with magnification G). The drawback of this magnification is the reduction of the field of view imaged in the plane (x–y)

somewhat compensated for by the capability of the 'inverse problem' approach to detect out-of-field droplets [21]. The magnification factor depends on the longitudinal coordinate z_k of the particle k. This geometrical magnification G_k [33] is given by

$$G_k = \frac{l_S + l_0}{l_S - z_k}, \tag{1}$$

where l_S, l_0 denote the distances from the point source to the calibration plane (O, x, y) and from the calibration plane to the sensor, respectively (figure 5). During the reconstruction procedure, this varying magnification must be taken into account to estimate the actual coordinates. To estimate this factor more accurately, we use a graduated calibration target (Reticle Edmunds Optics, F56-347) positioned in the injection plane. In this plane, the measured magnification is $G_0 = 1.42 \pm 0.005$, and G_k can be expressed as a function of G_0, l_0 and z_k in the form

$$G_k = \frac{G_0}{1 - (G_0 - 1)\frac{z_k}{l_0}}. \tag{2}$$

The relationship between the actual longitudinal coordinate z_k and that measured by digital holography z_k^{mes} is

$$z_k = -l_0 + \frac{z_k^{\mathrm{mes}} + l_0^{\mathrm{mes}}}{G_k}, \quad l_0 = \frac{l_0^{\mathrm{mes}}}{G_0}. \tag{3}$$

Thus G_k can be expressed from G_0, l_0^{mes} and z_k^{mes} as

$$G_k = G_0 + \frac{z_k^{\mathrm{mes}}}{l_0^{\mathrm{mes}}}(G_0 - 1). \tag{4}$$

The reconstructions presented in section 4 account for this non-uniform magnification.

The holograms of water droplets were recorded using a high-speed 10-bit CMOS NAC K4 digital camera, with 1280×1024 pixels of $21.7\,\mu\mathrm{m}$ size and a fill factor of 70%. The size of the sensor is therefore $27.77\,\mathrm{mm} \times 22.2\,\mathrm{mm}$. To minimize degradation due to external sources of distortion, no lens was mounted on the camera. Due to the divergence of the beam, the field of view is restricted to $19.5\,\mathrm{mm} \times 15.6\,\mathrm{mm}$. After 3D reconstruction of the droplets using the 'inverse problem' approach algorithm, the effective size is as large as $42\,\mathrm{mm} \times 40\,\mathrm{mm}$, which approximately corresponds to the area of the turbulence domain. Twenty-five time series of 1000 images were acquired at $1\,\mathrm{kHz}$ in full frame. The holograms of R114 droplets were recorded at higher frequency ($3\,\mathrm{kHz}$) using a high-speed 12-bit CMOS Photron SA5 digital camera, with 1024×1024 pixels of $20\,\mu\mathrm{m}$ size and a fill factor of 65%. The effective size of the reconstructed field is approximately the same as that with water droplets. The recording time of each time series is also $1\,\mathrm{s}$. In both cases, setups (diverging reference wave and camera) were calibrated by reconstructing the graduated calibration target located in the plane $(x, y, z = 0)$. Each hologram of the time series is reconstructed using the algorithm, detailed in section 3. This reconstruction provides the instantaneous 3D positions and sizes of the droplets. The 3D trajectories of the droplets are then obtained from the positions measured at the various successive instants, via a tracking method. Many tracking algorithms have been proposed in the literature to determine the Lagrangian trajectories of particles. The criteria upon which these algorithms are based vary from a few and simple to numerous and complex, depending on the type of flow investigated [34–36]. Here, the droplets in the turbulence domain being very diluted and the frame rate high, tracking is achieved by using a simple 3D nearest-neighbour criterion, which works well for this situation. A threshold on the maximum displacement was introduced

to handle incoming and outgoing droplets of the imaging field. Also, the positions z_{kt} along the beam axis were restricted to the range ($-25\,\text{mm} < z_{kt} < +25\,\text{mm}$), which corresponds to droplets located inside the turbulence domain. A very few pairing errors are generated by this tracking method. They occur exceptionally when two droplets with crossing trajectories move close to each other. In these cases, a three-frame minimum acceleration criterion [34] was used to find the right pairing.

3. Image processing of holograms

3.1. 'Inverse problem' approach algorithm

3D reconstruction of digital holograms is classically performed in two steps. The first step is based on a numerical simulation of the optical reconstruction. A 3D image volume is obtained by computing the diffracted field in planes located at increasing distances z from the hologram. Different techniques to simulate diffraction have been proposed (Fresnel transform [17], fractional Fourier transform [37, 38] and wavelets transform [39, 40]). The second step consists of segmenting, i.e. localizing and sizing each object in the obtained 3D image. The best focusing plane for each object has to be detected. Various criteria have been suggested in the literature. The limitations encountered in such approaches have been well identified [23]. The most restrictive are the poor depth accuracy and the limited field of view due to border effects.

In this framework, Soulez *et al* [20, 21] proposed an algorithm for parametric objects (objects whose shape can be described by a few parameters) 3D reconstruction, avoiding 3D volume reconstruction. This hologram analysis amounts to diffraction-pattern detection. The expression of the diffraction pattern of a spherical particle with a given size and location is well known in the far-field case [41] and easy to compute (direct problem). In our experiment, particles are spherical; therefore the diffraction pattern depends on only four parameters: their 3D location (x_k, y_k, z_k) and diameter (d_k). The inverse problem consists in reconstructing the set of droplets (locations and sizes: $\{x_k, y_k, z_k, d_k\}_{k=1,...,n}$) whose computed diffraction pattern best matches the real hologram. Finding this set is equivalent to a global optimization problem in which the difference between the diffraction model and the data (hologram) is minimized through a penalty function. Practically, this global optimization problem is solved by an iterative algorithm that alternates the coarse location of the droplets, refinement by local optimization and subtraction of the pattern from the hologram (cleaning step) [20].

As the diffraction pattern of each droplet is affected by the patterns due to the others, repetition of the processing over the residual images (obtained after cleaning) enables droplets with faint diffraction signatures to be detected and located, in particular those out of the field of view. This was shown both on synthesized and on real holograms (jet of $90\,\mu\text{m}$ diameter droplets). The benefits of the 'inverse problem' approach are discussed in detail in [23]. This approach gives improved particle location precision, in particular along the depth dimension, and increases the size of the effective transverse field of view. A notable drawback of the 'inverse problem' approach is the longer processing time required compared to conventional hologram reconstruction methods.

The computational complexity is increased for several reasons: particles are detected one at a time (the process is repeated for each particle, so the processing time increases linearly with the number of particles); out-of-field particle detection requires computing convolutions over larger images; matched-filter-type particle detection requires about twice as many convolutions

as for back-propagation; local optimization for sub-pixel accuracy is costly. On a standard desktop computer (3 GHz processor, single thread), the detection and location of a single particle in a hologram (with field expansion) requires about 5 min, and a series of 1000 holograms about 2 weeks of computations. For holograms with an average of five droplets like here, the reconstruction without out-of-field detection with an 'inverse problem' approach is about 15 times longer than with standard hologram processing techniques.

Accelerating the 'inverse problem' approach is currently ongoing work. Several ways are possible for that. Holograms can be processed in parallel using batch processing on several cores/nodes. In the case of holograms with many more particles, detecting several particles at a time is an efficient way to save computations. Finally, except for the discovery of new particles, the processing time can be significantly decreased if the tracking algorithm is used for the coarse detection of the particles on the next frame.

3.2. Wake masking for robust estimation

In the evaporating case, a wake image can be seen on the diffraction patterns of each droplet. These wakes, whose nature and physical interest are discussed in detail in section 4.2, disturb the signal. In this section, we show how to reduce the wake's influence on the measurements.

A distinctive feature of the digital holography technique is that the signal of an object is non-localized (i.e. is spread over the whole sensor). This important feature leads to the 3D reconstruction of out-of-field objects [21] or of a part of a hologram (considering some missing data). The 'inverse problem' approach algorithms take into account a confidence degree on each pixel by using a weighted mask depending on the pixel noise variance. In the case when the noise is assumed to be constant over all known pixels, the weighted mask can be viewed as a binary mask on the data: equal to 1 if the pixel is measured and to 0 otherwise. This mask weight allows wake disturbance on the freon hologram to be reduced.

Freon droplets are spherical objects whose hologram formation model is well known: the model consists of a diffraction pattern with radial symmetry. It is a chirp function whose amplitude is modulated by a Jinc function. The object's depth is encoded in the pattern frequency modulation, while the radius information is encoded in the amplitude modulation. The wake has a nearly constant thickness (about 60 pixels) and an origin located at the pattern centre. Therefore, the wake disturbs the low frequencies of the signal (recorded on the small-radius rings) more than the high frequencies (recorded on large-radius rings). Note that it has been shown [42] that the high frequencies of the signal are of lower magnitude than the low frequencies, but participate in accurate measurement (as they are more sensitive to changes in z and are recorded on more pixels). In order to reduce the influence of wakes on the hologram analysis, we chose to refine our measurements by repeating the 'inverse problem' approach algorithm using a mask suppressing the low-frequency part of the signal whose signal-to-noise ratio is weak due to the wake. The mask therefore consists of discs centred on the pattern centre (see in figure 6)

A first iteration of the algorithm gives us a rough estimate of the droplets parameters (x_k, y_k, z_k, d_k). A refinement step of this measurement is carried out using a mask of weight 0 on a disc centred on the approximate x_k, y_k positions of the droplets and radius equal to the size of the wake. With this choice of radius only rings for which the wake disturbs less than 25% of the pixels are considered. This second step could possibly be further improved by building the mask from a segmentation of the wake.

(a)　　　　　　　　　　　　　　　　(b)
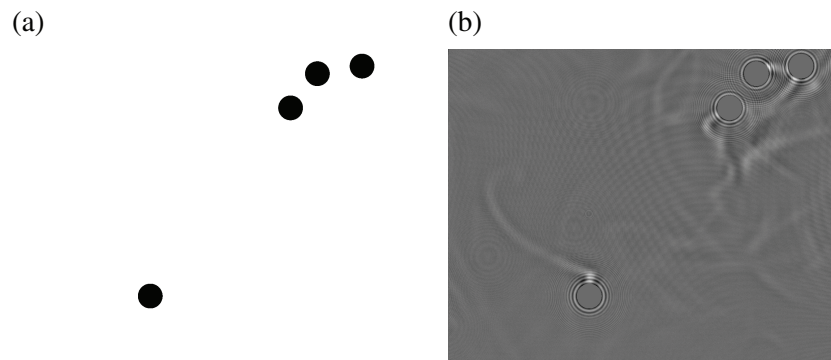
Figure 6. (a) An example of a binary mask. (b) The mask applied to the hologram.

(a)　　　　　　　　　　　　　　　　(b)
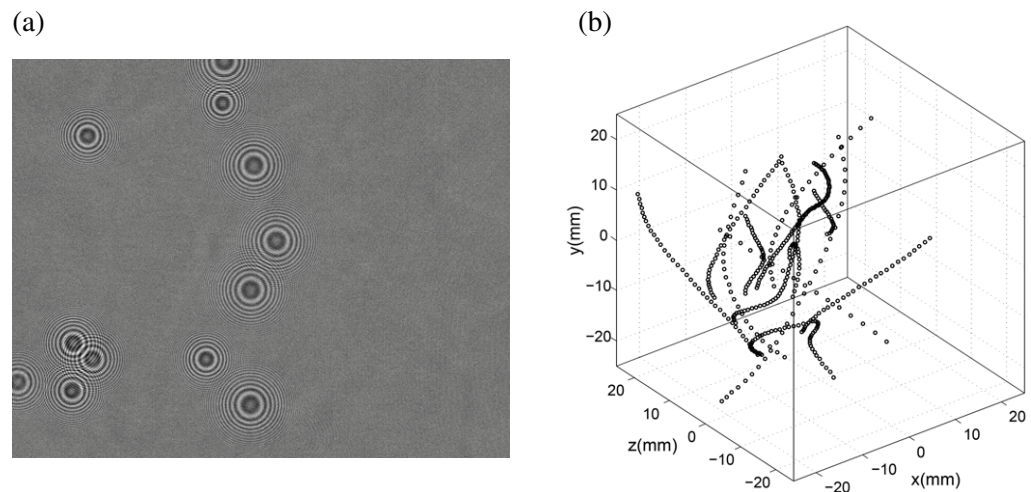
Figure 7. (a) A typical hologram of $60\,\mu$m water droplets, acquired with the high-speed 1280×1024 NAC K4 digital camera. (b) An example of 3D reconstructed tracks of $60\,\mu$m water droplets dispersing inside the turbulence domain.

4. Results

4.1. The case without appreciable evaporation: water droplets

A typical hologram of water droplets can be seen in figure 7(a).

　　About 1000 3D tracks of droplets inside the turbulence domain have been reconstructed (see the illustration in figure 7(b)). This required the processing of about 10 000 holograms. The length of these tracks ranges from 2–3 ms (2–3 time steps) to 40 ms, with an average of about 13.3 ms. This average, of the order of 8 Kolmogorov time τ_k and 0.3–0.4 integral time T_L, represents the mean residence time τ_r of the droplets inside the turbulence domain. This means that droplets are tracked for durations that cover the small time scales, in the range extending up to half the largest time scale of the flow. The statistics which is then inferred from these tracks is therefore restricted to these small time scales. In terms of spatial scales, the length of the tracks

ranges from 2–3 to 60 mm, with an average of about 13.7 mm. This average is of the order of 86 Kolmogorov length η_k and 0.3 integral length Λ. Only a few tracks, among the longest, have a length comparable to Λ and sometimes a bit larger.

The uncertainties on the lateral positions, δ_x, δ_y, and the depth position, δ_z, estimated from the holograms reconstruction have been determined theoretically by calculating the standard deviation σ_x, σ_y, σ_z of the estimates [42]. Following this approach, the accuracy attainable on the droplet positions is at best equal to the Cramer–Rao lower bounds [43, 44]. These bounds depend on the parametric model of the signal used in the reconstruction algorithm (diffraction patterns) and on the level of noise in the hologram. These lower bounds have been calculated for values of the parameters close to our experimental conditions. The number and the size of the pixels $\Delta\xi$, the fill factor, the imaging distance, the size d and the position of the droplets are taken into account in the calculation. We thus find that accuracy is at best $\sigma_x \simeq \sigma_y \simeq 3\,\mu$m, i.e. $\simeq d/20 \simeq \Delta\xi/14$, for the lateral positions, and $\sigma_z \simeq 60\,\mu$m, i.e. $\simeq d \simeq 3\Delta\xi$, for the depth position. In reality, accuracy on positions is probably not as good due to the presence of noise not taken into account in the theoretical estimates (background noise and noise due to interference between the diffraction patterns of the particles). The fact that uncertainty is higher in the depth direction is a classical problem with a single camera in-line holography setup with a small numerical aperture [45]. However, this uncertainty can be decreased to a value approaching that of the lateral directions by filtering the trajectories, as shown below. To compute the velocity and acceleration statistics, the positions along the tracks must be differentiated once or twice, respectively, and this would severely amplify the noise. Velocities and accelerations have been computed both with and without filtering. The filtering method is the same as that proposed by Mordant *et al* [9]. In practice, the spatial coordinates of the particle are convolved with a Gaussian kernel, which is differentiated once to obtain the velocity and twice for the acceleration. This convolution is equivalent to low-pass filtering of the trajectories to filter out the noise resulting from the position uncertainties. In the x and y directions where accuracy on positions is high, the effect of such filtering is very limited. This is illustrated in figures 8(a) and (c), where the non-filtered x components of the acceleration and velocity (dashed lines) fit the ones obtained by filtering (solid lines) well. In contrast, the beneficial effect of the filtering algorithm on the accelerations and velocities is clearly visible along the longitudinal z-direction, where the uncertainties on positions are much higher (figures 8(b) and (d)).

The PDFs of the three fluctuating velocity components computed with filtering are plotted on a semi-log scale in figure 9(a). The statistics were obtained from 7000 samples and each distribution was normalized by its standard deviation. The distributions for the three components are approximately Gaussian with standard deviations which are close to each other: $\sigma_{vx} = 0.90\,\mathrm{m\,s^{-1}}$, $\sigma_{vy} = 0.80\,\mathrm{m\,s^{-1}}$, $\sigma_{vz} = 0.78\,\mathrm{m\,s^{-1}}$. This Gaussian behaviour, which is expected for fluid particles in homogeneous isotropic turbulence [46, 47], was also reported by Snyder and Lumley [48] in the case of inertial particles (glass and copper particles) dispersing in a wind tunnel. It is noted that the data exhibit some scattering in the $[-3, 3]$ standard deviation range, even along the x and y directions, where the accuracy on location is high. This scattering is attributed to the low number of samples (1000 tracks) and the fact that PDFs are likely not converged. In comparison, the number of tracks currently used for Lagrangian statistics in other works with high Re_λ [12, 49, 50] is typically of the order of 5000–30 000, representing sometimes up to 10^8 samples. An asymmetry appears for high speeds along the x and z directions, which manifests itself by higher skewness in these directions. However, the statistics is not sufficient to draw any conclusion on this asymmetry.
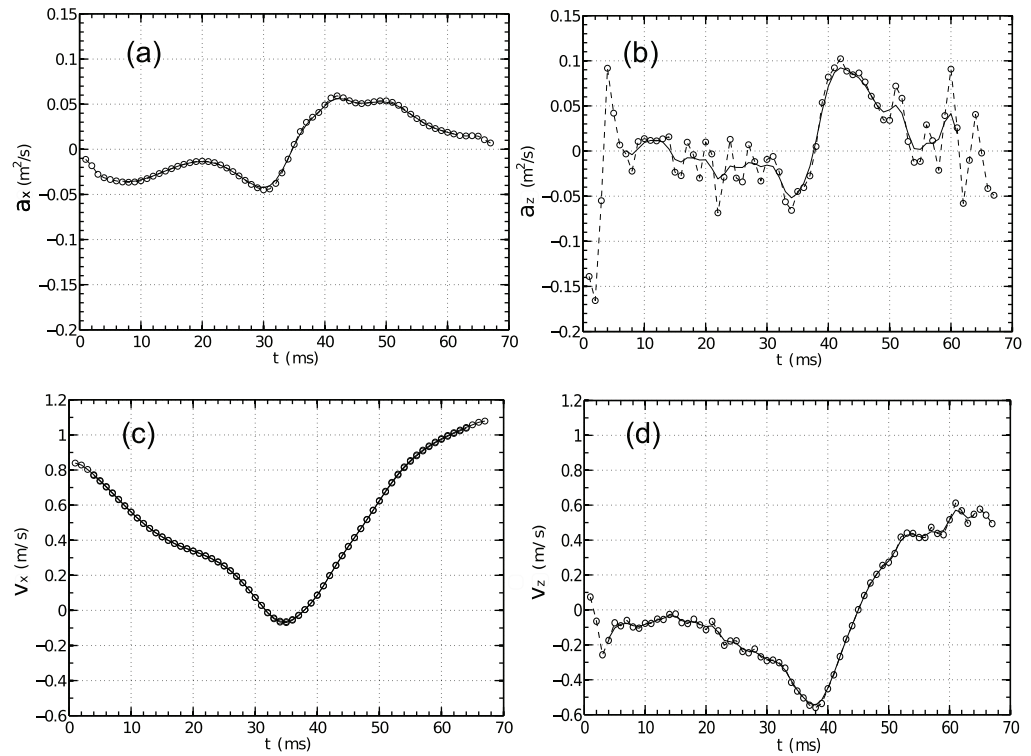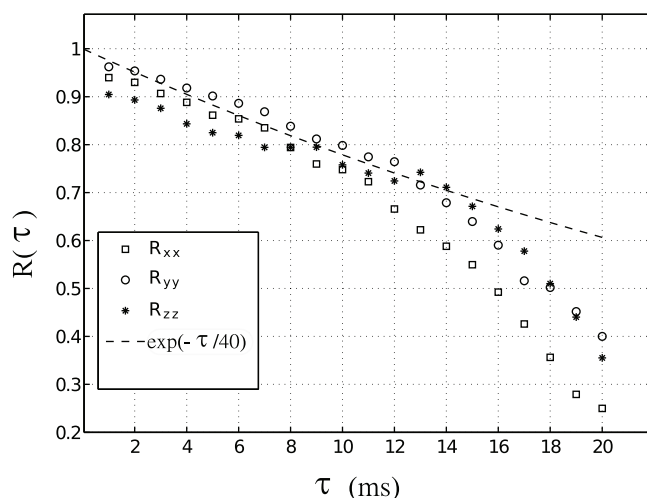
Figure 8. Velocity and acceleration components of a water droplet before and after filtering. v denotes the velocity and a the acceleration. x components are plotted on the left-hand side (panels (a) and (c)), while z components are plotted on the right-hand side (panels (b) and (d)). Open circle: raw data; solid line: filtered data.
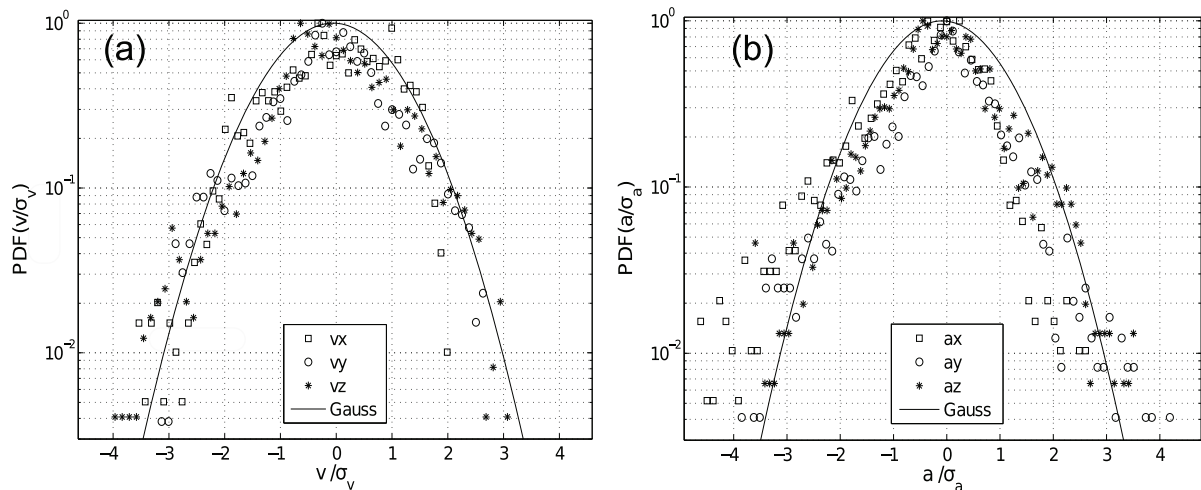
Figure 9. (a) PDFs of the water droplets' velocity fluctuations and (b) accelerations after z filtering.

Figure 10. Velocity auto-correlation functions of water droplets.

The PDFs of the three acceleration components are presented in figure 9(b). As expected, without filtering, the variance of the z component was found to be higher than in the other two directions due to the lower accuracy on the longitudinal position. The initial rms value was $\sigma_{az} = 88 \, \text{m s}^{-2}$ for the longitudinal component, compared to $\sigma_{ax} = 46 \, \text{m s}^{-2}$, $\sigma_{ay} = 47 \, \text{m s}^{-2}$, for the transversal ones. The filtering step reduces the variance of the longitudinal position estimation, leading to comparable values of acceleration in each direction: $\sigma_{ax} = 43 \, \text{m s}^{-2}$, $\sigma_{ay} = 44 \, \text{m s}^{-2}$, $\sigma_{az} = 55 \, \text{m s}^{-2}$. As is seen in the figure, the PDFs of the three components normalized by their rms values superpose rather well. Compared with a Gaussian with the same variance (solid line), they seem to have an exponential form. But the tails do not extend very far, as is reported for this Re_λ [8]. This can be attributed to various combined reasons. The number of tracks being small compared to that required in acceleration Lagrangian statistics, the scarce strong events, whose probability is smaller than 10^{-3}, are hardly measured. These strong events are even more difficult to see because the residence time of the droplet is short; hence long trajectories are not numerous. Also, the Stokes numbers of the droplet are larger than unity, so they do not respond rapidly to turbulence fluctuations, thus causing the turbulence effect to be filtered [51]. Finally, the time between samples (1 ms), typically of the order of Kolmogorov's time (1.6 ms), is still too long to measure these strong accelerations.

The Lagrangian velocity autocorrelation coefficients were computed by taking into account the bias corrections introduced by Mordant *et al* [12]. This bias arises from the fact that the tracks are not of the same length and that generally the longest ones correspond to the slowest particles. To limit this bias, the authors proposed to normalize the coefficients calculated at time τ by the velocity variance of recorded tracks whose duration is longer than τ. For the x component of the Lagrangian velocity this reads

$$R_{xx}(\tau) = \frac{1}{\sigma_{vx}^2(\tau)} \langle (V_x(t + \tau) V_x(t) \rangle, \tag{5}$$

where $\langle \rangle$ denotes the average over the tracks that contribute to $R_{xx}(\tau)$, and $\sigma_{vx}^2(\tau)$ is the variance of x component velocities estimated from these tracks. The result is plotted in figure 10. The correlation functions seem to decrease with two different characteristic time scales, the limit between the two types of behaviour corresponding to the mean residence time of the droplet
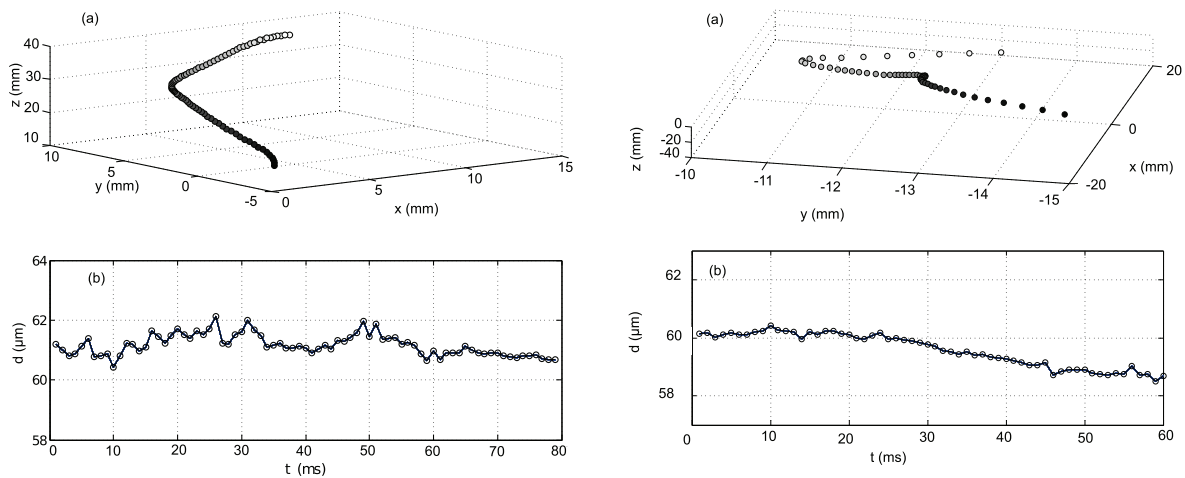
Figure 11. (a) Typical example of a water droplet trajectory and (b) of the Lagrangian time evolution of its diameter. Symbols from black to white: increasing time.

in the turbulence domain. However, the behaviour at long times must be considered with great care because the number of tracks is too low for the statistics to be meaningful. Fitting the beginning of the plot by a decaying exponential leads to a characteristic time of 40 ms, in good agreement with the estimations of the Lagrangian time given in section 2.1. Note that it is extremely difficult to evaluate the error on the unbiased correlation function thus estimated because it combines the velocity statistics and the lengths of the tracks. Referring to [52], it is reasonable to state that the variance of this estimation should vary as $1/\sqrt{N(\tau)}$, where $N(\tau)$ is the number of tracks used for the calculation at τ. On this basis, the error on $R_{xx}(\tau)$ is expected to increase by a factor of 2 in the range [1–13 ms] and a factor of 4 in the range [1–23 ms].

To study the evaporation of droplets from a Lagrangian point of view, it is essential to measure the diameter along the track with high accuracy. The tests performed with water droplets prove that the sizing accuracy of the in-line digital 'inverse' method used here fulfils this condition well. Typical tracks with Lagrangian diameter measurements are presented in figure 11. The figures referenced by (a) correspond to the space positions of the droplet plotted chronologically as a function of time with symbols from black to white. The value of the droplet's diameter at each time step is given in the figures located below (b). Since water droplets are at ambient temperature, under atmospheric pressure, no appreciable evaporation is expected while they remain in the turbulence domain. Moreover, the droplets being released in a limited number, the laden flow is quite dilute so that no coalescence is expected. Their diameters should therefore remain constant, which is the case with the illustrative examples. The small-diameter deviations observed along each track can be attributed to the noise measurements, which depend on various factors such as the quality of the hologram of the droplets, their position regarding the sensor: in-field or out-of-field, etc. A detailed discussion of the parameters influencing the accuracy of the diameter measurements with the 'inverse method' can be found in [20, 21]. This accuracy was theoretically estimated (using the Cramer–Rao lower bound computation [42]) at 1% for our operating conditions. Several factors contribute to particle sizing accuracy: the particle size, the location with respect to the hologram and the hologram signal-to-noise ratio. As
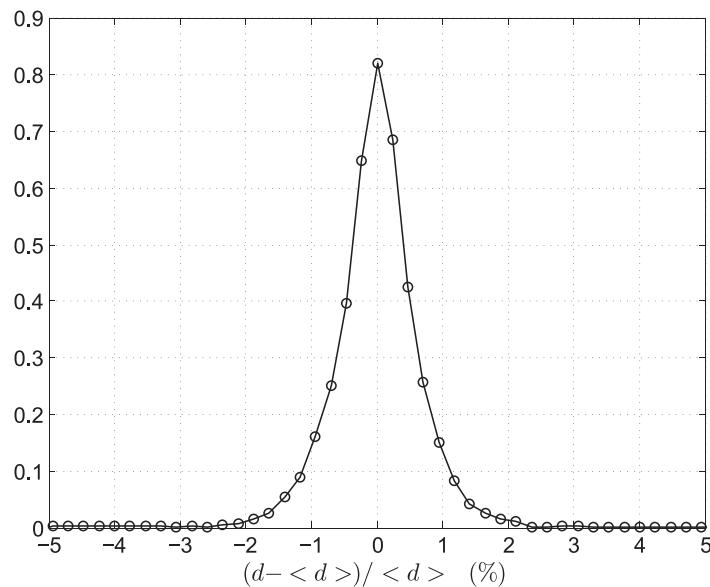
Figure 12. Distribution of the relative diameter deviations along the Lagrangian tracks. The relative diameter deviation is the difference between the diameter along a track and the mean diameter, divided by the mean diameter. $\langle d \rangle = 58.9\,\mu$m; rms standard deviation $\pm 1.6\%$.

the real signal-to-noise ratio was not taken into account in this theoretical estimation, accuracy on diameters is in reality not as good.

To evaluate the real accuracy on the diameter measurements along the tracks, the same method as in Lu *et al* [14] was used. This consists in computing the distribution of the relative diameter deviations along the Lagrangian tracks. For each track, this deviation is the difference between the diameter d measured at each time step and the mean diameter $\langle d \rangle$ along that individual track, divided by this mean diameter, that is, $(d - \langle d \rangle)/\langle d \rangle$. The result for the full dataset is displayed in figure 12.

The remarkable point is that deviations do not exceed 2% for the 1000 tracks reconstructed in the domain, showing that accuracy on the diameter is close to the value estimated theoretically. As a comparison, in a turbulence box and with initial polydispersed droplet spray (60–120 μm), Lu *et al* [14] obtained a distribution with a relative deviation of the order of $\pm 10\%$ with maxima of the order of 20%. The setup and the accuracy of the method being validated in the non-evaporating case, freon droplets were then injected.

4.2. Evaporating freon droplets

A striking and quite unexpected feature is the presence of a wake image on each hologram of a freon droplet. This wake image does not focus in the z-plane when the hologram is reconstructed, showing that it is not created by diffraction. It results from the deviation of the light by refractive index gradient located near the droplets, and thus is rather similar to an image obtained by a shadowgraphy or a Schlieren technique (phase information). The refractive index gradient has *a priori* two origins: either a concentration wake formed by the freon's vapour or a temperature wake formed by the air cooled by the droplet, both being possible.
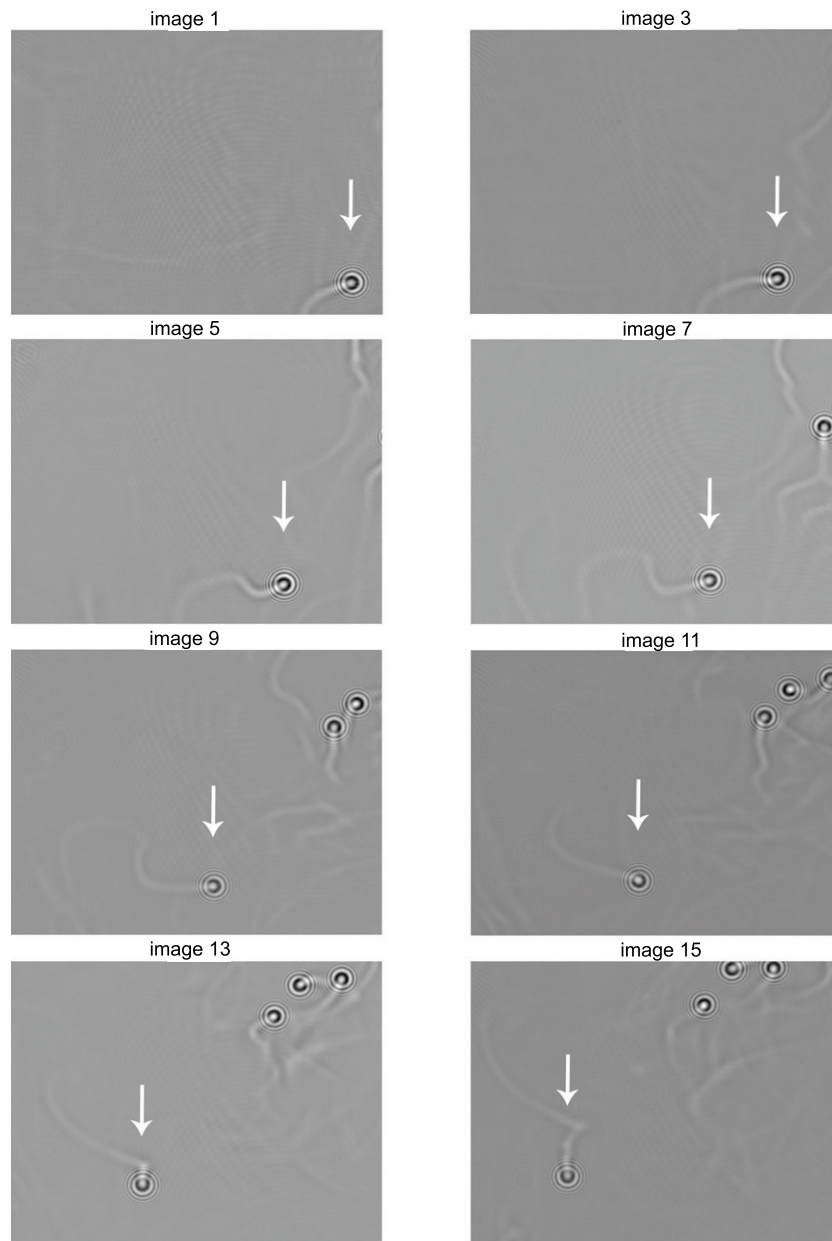
Figure 13. Holograms of freon droplets recorded at 1 kHz. The time between two successive images is 2 ms. The droplet marked with an arrow moves toward the left, while its wake is at each instant aligned with the relative velocity fluctuations seen by the droplet.

Before discussing this point, one can see in figure 13 that the behaviour of the wake relative to the droplet's trajectory provides a number of interesting results. The most remarkable one is that the wake is not aligned with the trajectory at each instant. This clearly appears when following the droplet marked by an arrow on the successive images (frame rate 1 kHz). The droplet is moving toward the left, while the wake, first aligned with this direction, turns upward, perpendicular to the trajectory (images 13–15). This shows that the droplets have
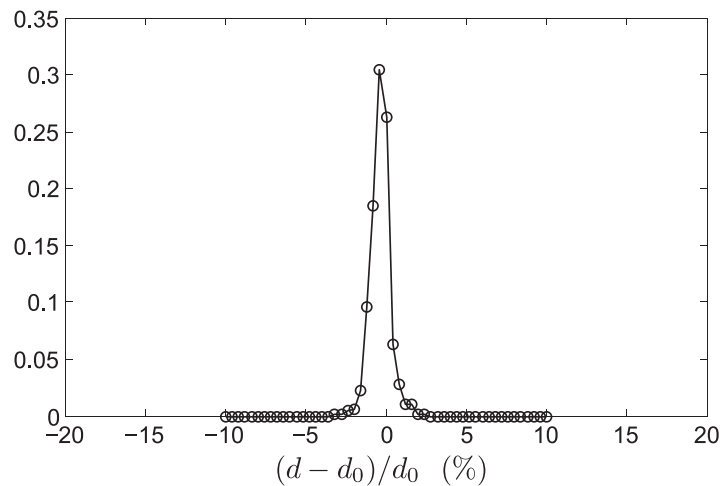
Figure 14. Distribution of relative freon droplet diameter deviations along Lagrangian tracks (statistics on 63 tracks). The relative diameter deviation is the difference between the diameter along a track and the initial diameter d_0, divided by the initial diameter.

inertial behaviour, and so, do not follow the fluids trajectories. The Lagrangian fluid motion about a droplet is therefore visualized. This result is consistent with the size of the droplets injected. As mentioned in section 2.3, we did not succeed in obtaining stable injection modes because of some instabilities in the process of freon liquefaction and hoarfrost problems at the capillary tip. As a result, the droplets released in this case (figure 4) are polydispersed with an average diameter of about 243 μm, much higher than that of the water droplets. Their response time is typically of the order of $\tau_d = 230$ ms, while the Stokes number is $St_k = \tau_d/\tau_k \approx 144$. Hence, they are strongly inertial. Perhaps a more sophisticated injection system, such as that used for instance by Gouge and Fisher (1997) [53] to jet cold xenon droplets in another context, would help to solve the problem.

The second remarkable result is, whatever the nature of the wakes (temperature and/or concentration), their lifetime is sufficient to follow their 2D spatial evolution (images 7–15 in the top right-hand corner). This provides a way to investigate how the topology of the concentration/temperature field is built, which is a particularly important issue regarding evaporation and combustion applications.

The most important information that sheds some light on the nature of the wake is the distribution of the relative diameter deviations along the Lagrangian tracks (figure 14). Due to the difficulty encountered in injecting the fluid, the number of tracks reconstructed is only 63. The distribution remains centred around zero, with deviations which do not exceed 2%, as in the case of water. It is deduced that on average practically no evaporation takes place on the time scales that the freon droplets reside in the sample volume and that the wakes are essentially thermal wakes, made up of the air cooled by the R114 freon droplets at a temperature close to 0°C. This result is not surprising. As the droplets are strongly inertial, they mostly follow ballistic trajectories, resulting in a residence time that is too short (11.7 ms) for evaporation to become significant. This is confirmed by a simple estimation of the heating time τ_h necessary for the vaporization state to be reached. The initial conditions at the droplet surface (temperature and vapour pressure) when entering the field of view are difficult to find

(a)

(b)
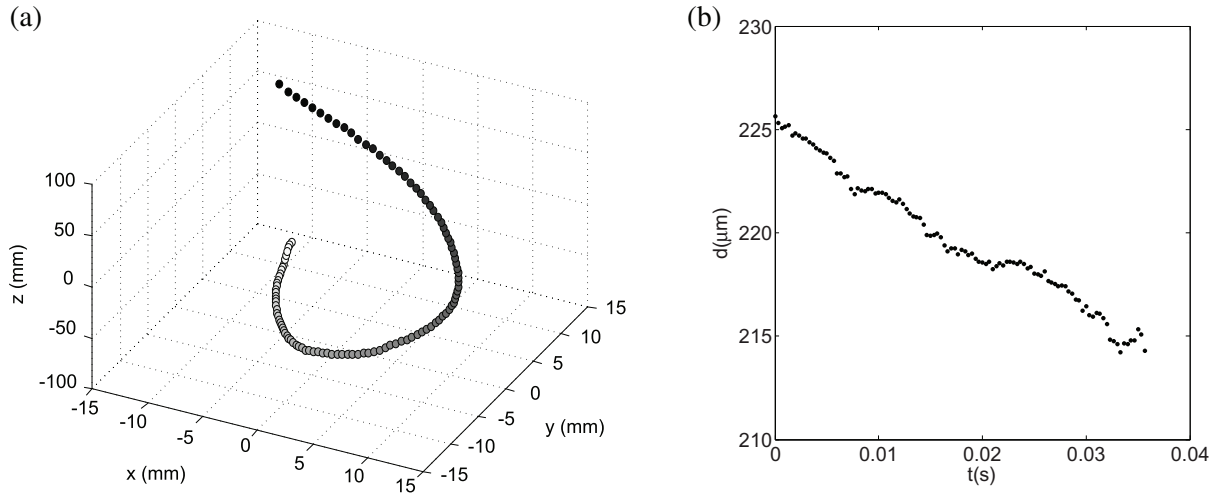
Figure 15. (a) The trajectory of the freon droplet that remains longest in the turbulence domain. Time increases from black to white. (b) Evolution of its diameter as a function of time.

out accurately. Supposing that the temperature is the same as that inside the injector: $T_0 \approx 0°$ C, the droplet is isolated in an atmosphere at $T_\infty \approx 25°$C at rest and the temperature within the droplet is homogeneous at each instant (infinite conductivity model), then the heating time can be estimated by [54]

$$\tau_h \approx -\frac{\rho_l C_l d_0^2}{12\lambda} \ln\left(\frac{T_{sat} - T_\infty}{T_0 - T_\infty}\right), \tag{6}$$

where $\rho_l = 1528 \, \text{kg m}^{-3}$ is the density and $C_l = 0.96 \, \text{kJ kg}^{-1} \, \text{K}^{-1}$ the specific heat of the liquid, $\lambda = 0.96 \, \text{mW m}^{-1} \, \text{K}^{-1}$ the thermal conductivity of the air, d_0 the initial diameter of the droplet and $T_{sat} = 3.8 \, °\text{C}$ the saturation temperature in these working conditions. For R114 droplets with an initial diameter of $243 \, \mu\text{m}$, this yields $\tau_h \approx 45$ ms, which is much greater than the average residence time in the domain.

However, some evaporation is measured on one of the longest trajectories inside the field of view (figure 15(a)). As can be noted in figure 15(b), the diameter along the trajectory decreases by about $10 \, \mu\text{m}$ in 35 ms, which corresponds to an evaporation rate $k_m = 1.29 \times 10^{-7} \, \text{m}^2 \, \text{s}^{-1}$. This evaporation rate is much smaller than the theoretical value $k_{th} = 6.9 \times 10^{-7} \, \text{m}^2 \, \text{s}^{-1}$ that can be estimated by using the classical steady-state approach of Spalding's law [55]. This suggests that the temperature of the droplet has not reached the saturation temperature and that the evaporation process is not maximum. The concentration of vapour at the surface is likely to be low and even in that case, the image wake should be mostly caused by a gradient of temperature.

4.3. Inferring Lagrangian fluid motion about a droplet

Since the wake corresponds to the air cooled by the droplet, it should be approximately aligned with the instantaneous relative velocity seen by the droplet. An attempt was made to validate this point. Digital holography does not provide any information on the air velocity around the droplet. A complementary technique such as PIV would be necessary for that. However, we tried to estimate this relative velocity theoretically by using a dynamical equation for the droplet.

Supposing, for the sake of simplicity, that the main forces acting on it reduce to gravity and the drag force, this equation is written as (see, for instance, [56])

$$\frac{d\mathbf{u}_d}{dt} = \left(1 - \frac{1}{\gamma}\right)\mathbf{g} + \frac{3C_D(Re_d)}{4d\gamma}|\mathbf{u} - \mathbf{u}_d|(\mathbf{u} - \mathbf{u}_d), \tag{7}$$

where γ is the ratio of densities ρ_l/ρ_a, $\mathbf{u}_d$ the droplet velocity, $\mathbf{u}$ the air velocity and Re_d the Reynolds number based on the droplet diameter and the relative velocity $\mathbf{u}_r = \mathbf{u} - \mathbf{u}_d$. The Reynolds number for this size of droplet is in the range $0 \leqslant Re_d \leqslant 800$, so the drag coefficient is well described by the empirical correlation

$$C_D(Re_d) = \frac{24}{Re_d}(1 + \beta Re_d^\alpha), \tag{8}$$

where $\beta = 0.15$ and $\alpha = 0.687$. The projection of this equation along the three directions of the holographic setup yields the system

$$\tau_d \dot{u}_{dx} = u_{rx}(1 + \beta Re_d^\alpha), \tag{9}$$

$$\tau_d \dot{u}_{dy}(1 - g) = u_{ry}(1 + \beta Re_d^\alpha), \tag{10}$$

$$\tau_d \dot{u}_{dz} = u_{rz}(1 + \beta Re_d^\alpha), \tag{11}$$

where $\tau_d = \rho_l d^2/18\mu_a$ and the symbol ($\dot{}$) denotes the time derivative. By summing the square of equations (9)–(11), one obtains

$$\tau_d^2(\dot{u}_{dx}^2 + \dot{u}_{dy}^2 + \dot{u}_{dz}^2) = u_r^2(1 + \beta Re_d^\alpha)^2. \tag{12}$$

τ_d, $\dot{u}_{dx}^2$, $\dot{u}_{dy}^2$ and $\dot{u}_{dz}^2$ have been calculated at each time step from the reconstructed trajectory (figure 15(a)) and the measured diameter (figure 15(b)), while the unknown of the system u_r^2 has been determined by finding the value solution of equation (12). Once u_r^2 has been determined, Re_d is known and the three components of the relative velocity can be readily deduced. The results are plotted in figure 16. The sequence represents holograms of the above droplet at various instants along its 2D trajectory in the plane x–y (solid line), together with its velocity in the plane (black arrow) and the relative velocity that is seen by this droplet in the same plane, determined by using equation (8) (white arrow). The variation in the grey levels of the background from one image to another is due to the image processing that was used to improve the contrast of the wake. As can be seen, the 2D relative velocity is rather well aligned with the x–y wake projection all along the trajectory. The differences which are observed can be attributed to uncertainties in computing the acceleration, in the diameter measurement and to the simplified dynamical equation. However, it is interesting to note (images at $t = 0.009$ and 0.021 s) that the sudden changes in the wake direction close to the droplet are well correlated with the sudden changes in the relative velocity direction. These trends are particularly promising for this technique, which could provide a simple way to obtain information on the gas around the droplet. It would be of course necessary to validate the trends in the other planes, which would require a second camera. These time sequence images illustrate well the off-frame particle detection capacity of the inverse method. The droplet is outside the field of view from $t = 0.009$ to 0.021 s; however, its off-frame presence is still detected and its location and diameter are measured, as shown in figure 15.
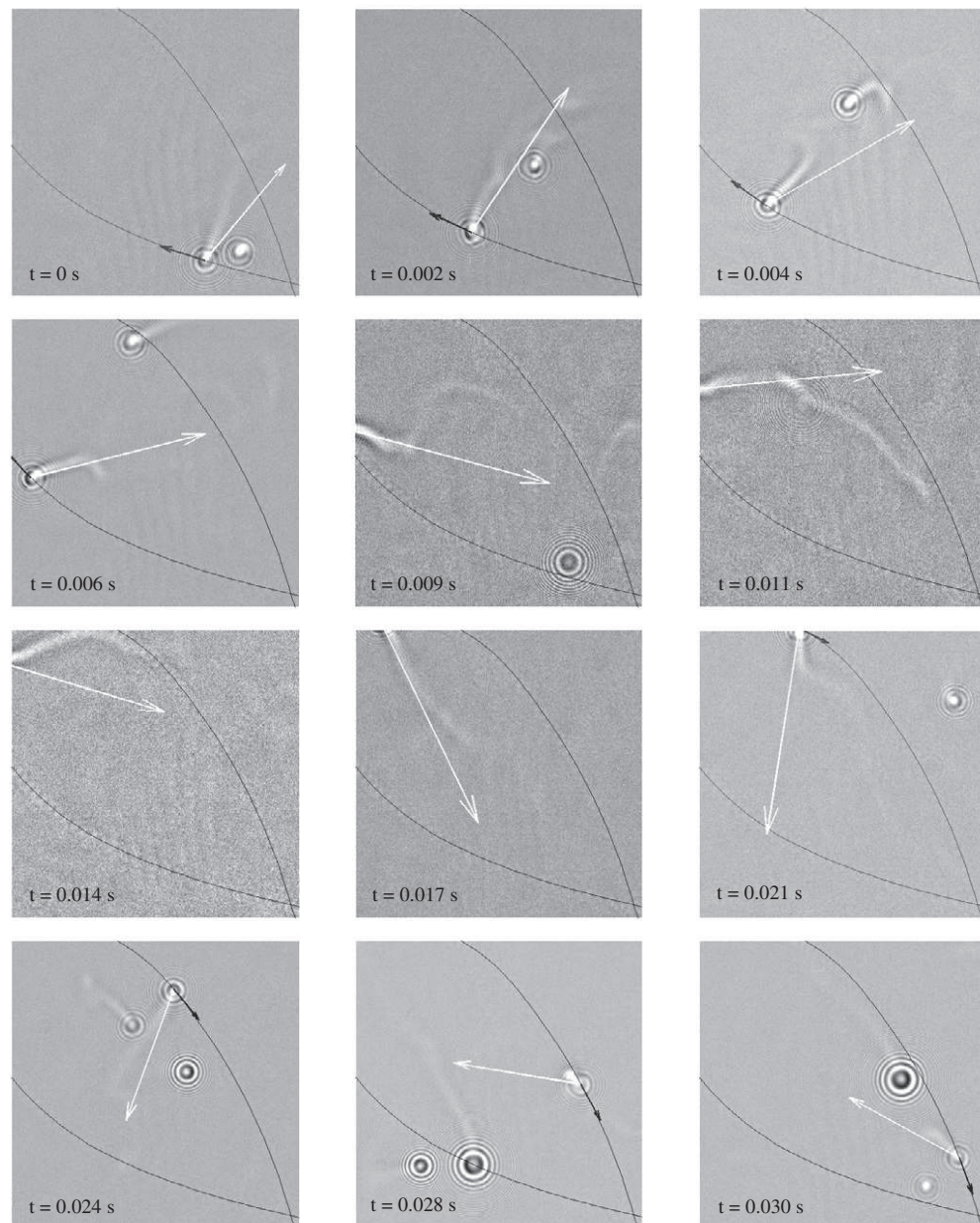
Figure 16. Time sequence images showing the evolution of the wake of a freon droplet in the x–y-plane and that of the relative velocity in this plane seen by the droplet (white arrow), calculated with equations (9) and (10) and the Lagrangian data. The solid line on each image represents the trajectory of the droplet and the black arrow its velocity. From $t = 0.009$ to 0.021 s, the droplet is out-of-field: its location and diameter are still measured thanks to the off-frame particle detection advantages of the inverse method.

5. Conclusion

The in-line digital holography technique tested is well suited for studying the evaporation of droplets in highly turbulent flows, from a Lagrangian point of view. This was shown by injecting monodispersed droplets in a homogeneous, nearly isotropic, strong turbulence domain (50 mm^3)

and by measuring their size evolution along their 3D trajectories from holograms taken with a single high-speed camera. The holograms have been reconstructed with an algorithm based on an original 'inverse problem' approach [20] that offers several advantages. It allows the detection of droplets located out of the field of view, a point that has been confirmed here. Lateral dimensions of the sample volume ($40 \times 40 \times 140\,\mathrm{mm}^3$) are about 2.5 times greater than when one is restricted to conventional hologram reconstruction and thus are large enough to investigate the turbulence domain. This approach is also known to improve the accuracy of the droplet depth position and diameter. Its main drawback is a longer processing time compared to conventional methods.

The gain in position and diameter accuracy have been checked with $60\,\mu$m water droplets, which do not appreciably evaporate on the residence time scales in the sample volume. Uncertainty on the depth position expected for our operating conditions ($60\,\mu$m for this drop diameter) is 20 times that on the transversal positions ($3\,\mu$m or about 1 pixel size), whereas it is typically of the order of 110 times ($\approx d/\lambda_{\mathrm{laser}}$) with a standard reconstruction algorithm [45]. But in reality, depth–position accuracy is not so good, due to the presence of noise. This appears on the PDFs of Lagrangian accelerations obtained from 1000 reconstructed trajectories, where we note that the rms value of the longitudinal component is twice the value of the transverse ones. Depth uncertainty can be decreased to a value approaching that of the transverse directions by using a filtering algorithm, of the type proposed by Mordant *et al* [9]. With filtering, the PDFs of the three acceleration components superpose pretty well, as expected in an isotropic flow. Accuracy on diameters has been estimated to be $\pm 1.6\%$ around their average value of $58.9\,\mu$m by computing their variance along each trajectory. Tests on evaporation have been performed with R114 freon droplets. Their residence time in the turbulence domain proved, on average, to be too short for evaporation statistics. This is explained by some injection problems resulting in larger droplets ($240\,\mu$m), with ballistic behaviour. However, a decrease in diameter has been measured on the droplet having the longest residence time. Very interestingly, a wake image created by a temperature gradient is present on each droplet hologram. This thermal wake originates from the air cooled by the droplets and is approximately aligned with the instantaneous relative velocity seen by the droplet. Its orientation, which visualizes the Lagrangian fluid motion about the droplet, compares rather well with that calculated by using a dynamical equation for describing the droplet motion. The space evolution of these wakes provides a way to investigate how the topology of the temperature/concentration field is built, which is a particularly important issue with regard to evaporation and combustion applications.

References

[1] Balachandar S and Eaton J K 2010 Turbulent dispersed multiphase flow *Annu. Rev. Fluid Mech.* **42** 111–33
[2] Reveillon J and Demoulin F X 2007 Effects of the preferential segregation of droplets on evaporation and turbulent mixing *J. Fluid Mech.* **583** 273–302
[3] Taylor G I 1921 Diffusion by continuous movements *Proc. Lond. Math. Soc.* **20** 196–211

[4] Toschi F and Bodenschatz E 2009 Lagrangian properties of particles in turbulence *Annu. Rev. Fluid Mech.* **41** 375–404

[5] Virant M and Dracos T 1997 3D PTV and its application on Lagrangian motions *Meas. Sci. Technol.* **8** 1539–52

[6] Bourgoin M, Ouellette N T, Xu H, Berg J and Bodenschatz E 2006 The role of pair dispersion in turbulent flow *Science* **311** 835–8

[7] La Porta A, Voth G A, Crawford A M, Alexander J and Bodenschatz E 2001 Fluid particle accelerations in fully developed turbulence *Nature* **409** 1017–9

[8] Voth G A, Laporta A, Crawford A M, Alexander J and Bodenschatz E 2002 Measurement of particle acceleration in fully developed turbulence *J. Fluid. Mech.* **469** 121–60

[9] Mordant N, Crawford A M and Bodenschatz E 2004 Experimental Lagrangian acceleration probability density function measurements *Physica* D **193** 245–51

[10] Mordant N, Crawford A M and Bodenschatz E 2004 Three-dimensional structure of the Lagrangian acceleration in turbulent flows *Phys. Rev. Lett.* **93** 214501

[11] Volk R, Mordant N, Verhille G and Pinton J-F 2008 Laser Doppler measurement of inertial particle and bubble accelerations in turbulence *Eur. Phys. Lett.* **81** 34002

[12] Mordant N, Lévèque E and Pinton J-F 2004 Experimental and numerical study of the Lagrangian dynamics of high Reynolds turbulence *New J. Phys.* **6** 116

[13] Gopalan B, Malkiel E and Katz J 2008 Experimental investigation of turbulent diffusion of slightly buoyant droplets in locally isotropic turbulence *Phys. Fluids* **20** 095102

[14] Lu J, Fugal J P, Nordsiek H, Saw E W, Shaw R A and Yang W 2008 Lagrangian particle tracking in three dimensions via single-camera in-line digital holography *New J. Phys.* **10** 125013

[15] Katz J and Sheng J 2010 Application of holography in fluid mechanics and particle dynamics *Annu. Rev. Fluid Mech.* **42** 531–55

[16] Xu L, Peng X, Guo Z, Miao J and Asundi A 2005 Imaging analysis of digital holography *Opt. Express* **13** 2444–52

[17] Kreis T M 2005 *Handbook of Holographic Interferometry, Optical and Digital Methods* (Berlin: Wiley-VCH)

[18] Gopalan B, Malkiel E, Sheng J and Katz J 2005 Diesel droplet diffusion in isotropic turbulence with digital holographic cinematography *FEDSM2005: Proc. of 2005 ASME Fluids Engineering Division Summer Meeting and Exhibition* (*Houston, TX,* 2005) (Houston, USA: ASME) pp 1–5 FEDSM2005-77423

[19] Hwang W and Eaton J K 2004 Creating homogeneous and isotropic turbulence without a mean flow *Exp. Fluids* **36** 444–54

[20] Soulez F, Denis L, Fournier C, Thiébaut E and Goepfert C 2007 Inverse-problem approach for particle digital holography: accurate location based on local optimization *J. Opt. Soc. Am.* **24** 1164–71

[21] Soulez F, Denis L, Fournier C, Thiébaut E and Goepfert C 2007 Inverse problem approach in particle digital holography: out-of-field particle detection made possible *J. Opt. Soc. Am.* **24** 3708–16

[22] Lee S H, Roichman Y, Yi G R, Kim S H, Yang S M, van Blaaderen A, van Oostrum P and Grier D G 2007 Characterizing and tracking single colloidal particles with video holographic microscopy *Opt. Express* **15** 18275–82

[23] Gire J, Denis L, Fournier C, Thiébaut E, Soulez F and Ducottet C 2008 Digital holography of particles: benefits of the 'inverse-problem' approach *Meas. Sci. Technol.* **19** 074005

[24] Goepfert C, Marié J-L, Chareyron D and Lance M 2010 Characterization of a system generating a homogeneous isotropic turbulence field by free synthetic jets *Exp. Fluids* **48** 809–22

[25] Sawford B L 1991 Reynolds number effects in Lagrangian stochastic models of turbulent dispersion *Phys. Fluids* **3** 1577–86

[26] Yeung P K 2001 Lagrangian characteristics of turbulence and scalar transport in direct numerical simulation *J. Fluid Mech.* **427** 241–74

[27] Yeung P K and Sawford B L 2001 Lagrangian statistics in uniform shear flow: direct numerical simulation and Lagrangian stochastic models *Phys. Fluids* **13** 2627–34

[28] Lin S P and Reitz R D 1998 Drop and spray formation from a liquid jet *Annu. Rev. Fluid Mech.* **30** 85–105

[29] Lee E R 2003 *Microdrop Generation* (Boca Raton, FL: CRC Press)

[30] Hwang W and Eaton J K 2006 Homogeneous and isotropic turbulence modulation by small heavy (St $\sim$ 50) particles *J. Fluid. Mech.* **564** 361–93

[31] Meng H, Anderson W L, Hussain F and Liu D D 1993 Intrinsic speckle noise in in-line particle holography *J. Opt. Soc. Am.* A **10** 2046–58

[32] Royer H 1974 An application of high-speed microholography: the metrology of fogs *Nouv. Rev. Opt.* **5** 87–93

[33] Amsler P, Stetzer O, Schnaiter M, Hesse E, Benz S, Moehler O and Lohmann U 2009 Ice crystal habits from cloud chamber studies obtained by in-line holographic microscopy related to depolarization measurements *Appl. Opt.* **48** 5811–22

[34] Ouellette N T, Xu H and Bodenschatz E 2006 A quantitative study of three-dimensional Lagrangian particle tracking algorithms *Exp. Fluids* **40** 301–13

[35] Cheung K, Ng W B and Zhang Y 2005 Three dimensional tracking of particles and their local orientations *Flow Meas. Instrum.* **16** 295–302

[36] Satake S, Kunugi T, Sato K, Kanamori H and Taniguchi J 2006 Measurement of 3D flow in a micro-pipe via micro digital holographic particle tracking velocimetry *Meas. Sci. Technol.* **17** 1647–51

[37] Pellat-Finet P 1994 Fresnel diffraction and the fractional-order Fourier transform *Opt. Lett.* **19** 1388–90

[38] Ozaktas H M, Arikan O, Kutay M A and Bozdagt G 1996 Digital computation of the fractional Fourier transform *Signal Process. IEEE Trans.* **44** 2141–50

[39] Lefebvre B C, Coetmellec S, Lebrun D and Ozkul C 2000 Application of wavelet transform to hologram analysis: three-dimensional location of particles *Opt. Lasers Eng.* **33** 409–21

[40] Liebling M, Blu T and Unser M 2003 Fresnelets: new multiresolution wavelet bases for digital holography *Image Process. IEEE Trans.* **12** 29–43

[41] Tyler G A and Thompson B J 1976 Fraunhofer holography applied to particle size analysis a reassessment *J. Mod. Opt.* **23** 685–700

[42] Fournier C, Denis L and Fournel T 2010 On the single point resolution of on-axis digital holography *J. Opt. Soc. Am.* A **27** 1856–62

[43] Rao C R 1945 Information and the accuracy attainable in the estimation of statistical parameters *Bull. Calcutta Math. Soc.* **37** 81–91

[44] Cramer H 1946 *Mathematical Methods of Statistics* (Princeton, NJ: Princeton University Press)

[45] Meng H, Pan G, Pu Y and Woodward S H 2004 Holographic particle image velocimetry: from film to digital recording *Meas. Sci. Technol.* **15** 673–85

[46] Batchelor G K 1949 Diffusion in a field of homogeneous turbulence, Eulerian analysis *Aust. J. Sci. Res.* **2** 437–50

[47] Pope S B 2000 *Turbulent Flows* (Cambridge: Cambridge University Press)

[48] Snyder W H and Lumley J L 1971 Some measurements of particle velocity autocorrelation functions in turbulent flow *J. Fluid Mech.* **48** 41–71

[49] Voth G A, Satyanarayan K and Bodenschatz E 1998 Lagrangian acceleration measurements at large Reynolds numbers *Phys. Fluids* **10** 2268–80

[50] Volk R, Calzavarini E, Lévèque E and Pinton J-F 2011 Dynamics of inertial particles in a turbulent von Karman flow *J. Fluid Mech.* **668** 223–35

[51] Bec J, Biferale L, Boffetta G, Celani A, Cencini M, Lanotte A, Musacchio S and Toschi F 2006 Acceleration statistics of heavy particles in turbulence *J. Fluid. Mech.* **550** 349–58

[52] Mordant N 2001 Mesure lagrangienne en turbulence: mise en oeuvre et analyse *PhD Thesis* École Normale Supérieure de Lyon

[53] Gouge M J and Fisher P W 1997 A cryogenic xenon droplet generator for use in a compact laser plasma x-ray source *Rev. Sci. Instrum.* **68** 2158–62

[54] Kuo K 1986 *Principles of Combustion* (New York: Wiley)

[55] Lefebvre A H 1989 *Atomization and Sprays* (London: Taylor and Francis)

[56] Michaelides E E 2006 *Particles, Bubbles and Drops: Their Motion, Heat and Mass Transfer* (Singapore: World Scientific)